Infrared Image Processing to Guide the Identification of Damage and Dissipative Mechanisms in 3D Layer-to-Layer Woven Composites

Libor Navrátil, Vincent Le Saux, Sylvain Leclercq, Nicolas Carrere, Yann Marco

Infrared image processing to guide the identification of damage and dissipative mechanisms in 3D layer-to-layer woven composites.

Libor Navrátil[1,2], Vincent Le Saux[1*], Sylvain Leclercq[2], Nicolas Carrere[1] and Yann Marco[1]

[1*]ENSTA Bretagne – Institut de Recherche Dupuy de Lôme (IRDL), UMR CNRS 6027, Brest France.
[2]Safran Landing Systems, Vélizy, France.

*Corresponding author(s). E-mail(s): vincent.le_saux@ensta-bretagne.fr;
Contributing authors: libor.navratil@ensta-bretagne.org; sylvain.leclercq@safrangroup.com; nicolas.carrere@ensta-bretagne.fr; yann.marco@ensta-bretagne.fr;

Abstract

This article discusses techniques that aim at facilitating the identification of dissipative mechanisms activated in woven composites under cyclic loadings. The focus is put on the post-processing of thermal measurements acquired during heat build-up experiments, as these are usually used to identify the dissipation sources. The importance of motion compensation pre-processing is demonstrated as it is shown that the latter enhances the quality of the evaluated thermoelastic and dissipation fields. Two specific post-processing techniques are presented in this article. The first one analyzes temperature or thermoelastic fields and searches to detect thermal events associated with the creation of cracks. The second one is based on a Fourier decomposition of thermal fields and aims at highlighting an increased contribution of friction as a dissipation source.

Keywords: 3D woven composite, infrared thermography, heat build-up, cyclic fatigue

1 Introduction

Infrared thermography is a contact free method providing full-field measurements of the surface temperature. This technique has been gaining popularity in material testing since it permits to gather information about thermal effects associated with deformation processes [1–3]. First observations focused on the thermoelastic effects induced by reversible volumetric straining of materials [4, 5]. For isotropic materials, these effects provide, under adiabatic conditions, a direct link between temperature variations and changes in the first stress (or strain) invariant. The experimental technique exploiting this phenomenon is called "thermoelastic stress analysis" and is widely used in fracture mechanics, damage detection, fatigue monitoring, and residual stress analysis. An overview of this technique can be found in [6]. Another widely addressed topic concerns the investigation of the heat involved in irreversible mechanical transformations. The associated constitutive model is usually based upon the framework of thermodynamics of irreversible processes [7]. This field of study is closely related to an expanding domain of applications concerning fatigue life predictions. As the traditional way of characterizing high cycle fatigue (HCF) properties is time consuming and expensive [8–11], alternative experimental methods based upon temperature measurements were developed to study the fatigue behaviour of materials [12, 13]. The main objective of these approaches is to accelerate this characterization process. One of the approaches consists in analysing the heat build-up response of the material under cyclic loadings. Even though the first studies focused mostly on metallic materials [14, 15], this technique was progressively adapted to other materials such as elastomers [16, 17] or short fibre reinforced composites [18, 19]. The analyses of the heat build-up response usually aim at evaluating the dissipated energy that is plotted against the strain or stress amplitude yielding the so-called heat build-up curve. The accuracy of the subsequent fatigue life predictions is determined by the accuracy of the modelling of the involved dissipating mechanisms that govern the fatigue failure. However, in order to be modelled correctly, they have to be properly identified first. This identification process is rather transparent when dealing with metallic materials, since the dissipative mechanisms involved are, generally, few and often limited to plasticity. Therefore, the description remains relatively simple and can be based on analyses of the average values of dissipated energy [20], $2\times$f lock-in component (component corresponding to the double of the excitation frequency) [21], etc. However, this description can quickly become complicated if multiple dissipative mechanisms have to be considered as in the case of composite materials. These materials usually possess a rather complex microstructure leading to several dissipative mechanisms that may include viscoelasticity, plasticity, damage or friction. Thus, in order to make use of all the information provided by full-field temperature measurements, it would be beneficial to extend the existing post-processing methods by implementing techniques that could guide the identification process.

This article presents post-processing techniques that aim at facilitating this identification of the dissipation sources. The use of these techniques is illustrated on a layer-to-layer woven composite material. In order to improve the precision of the subsequent post-processing, it is convenient to compensate the relative motion of the specimen when the latter is being loaded. The benefit of this pre-processing procedure is illustrated on the evaluation of dissipation and thermoelastic coupling fields as it is shown that the use of the motion compensation leads to lower residuals. Two specific post-processing techniques of thermal imaging were developed in this study. The first technique detects thermal events linked to the formation of cracks. The second technique, used when cracks have been created, is designed to highlight the areas with a high intensity of friction, generated by relative movements between crack faces.

In the following, the first section presents the material, the sample geometry, illustrates the loading protocols and details the experimental setup. The second section summarizes the analysis techniques used to post-process the experimental data. The third section discusses the performance of the new proposed techniques and their link to microstructure measurements. The fourth section is devoted to conclusions and perspectives.

2 Experimental settings

2.1 Material and samples

The material used in this study is a woven composite that is provided for research purposes by the Safran Group. This woven composite is an unbalanced layer-to-layer interlock consisting of 48k carbon fibre yarns consolidated with an epoxy resin. The composite microstructure consists of eight plies. The total thickness of the specimens is 7.5 mm. The coupons used in this study were machined out of composite panels fabricated by the resin transfer moulding process. The geometry and dimensions of these coupons are illustrated in figure 1. The latter depicts the region of interest investigated by the infrared observations (section 2.3) and the high emissivity markers used for motion compensation (section 3.1).

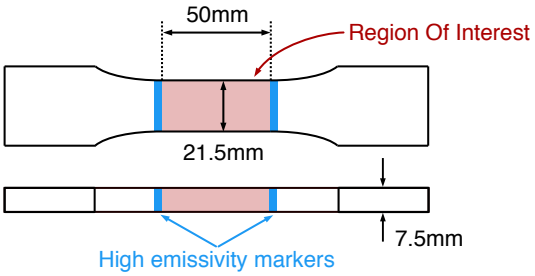

Fig. 1 Specimen geometry.

2.2 Loading protocol

All the experiments presented in this article were carried out on an INSTRON 1342 servo-hydraulic testing machine of a 100kN capacity. Two different loading protocols were employed (figure 2). Both protocols consist in applying a set of loading steps. The stress amplitude (defined as $\sigma_{amp} = (\sigma_{max} - \sigma_{min})/2$) is held constant during each step. The first type of protocol, called heat build-up protocol [16, 17, 22] involves the application of a sequence of loading steps of increasing stress amplitude. The second type of protocol, called reverse heat build-up protocol [23], applies a sequence of loading steps of decreasing stress amplitude. It should be specified that the stress always refers to the average

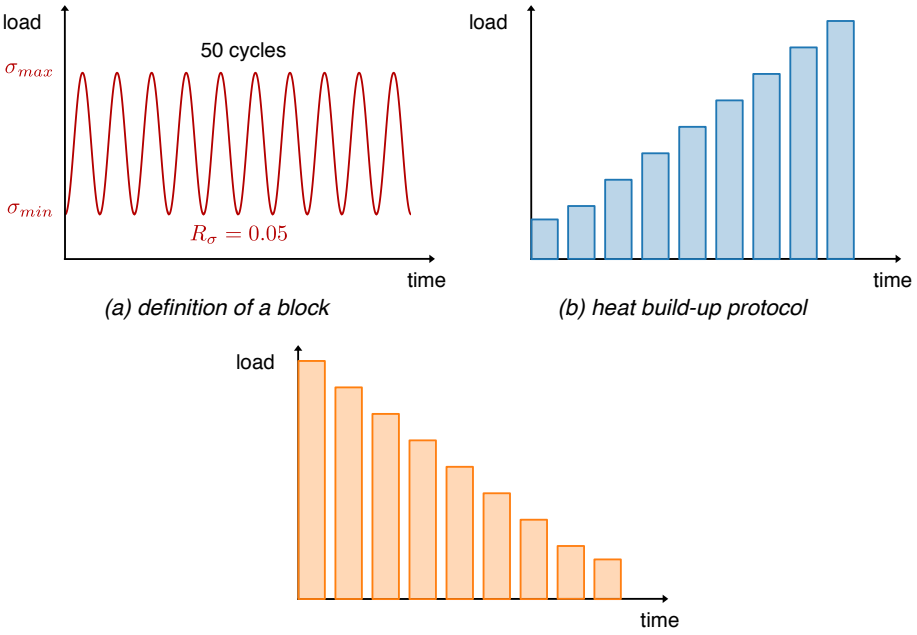

Fig. 2 Loading protocols.

stress applied to the specimen. The real stress distribution is heterogeneous due to the complex microstructure of the studied material and would, thus, be cumbersome to work with. The stress ratio used during the whole campaign is equal to $R_\sigma = 0.05$, the loading frequency was set to $f = 2\,\text{Hz}$ and kept constant. It is convenient to mention that other experimental campaigns applying mechanical frequencies up to 10 Hz were carried out. These results are available in [23].

For confidentiality reasons, all the stress results presented henceforth were normalized by an arbitrary value kept constant for the whole article.

2.3 Temperature measurements

The temperature measurements were carried out with a cooled InSb InfraTec ImageIR 10300 camera [24]. The Focal Plane Array is a matrix of 1920×1536 detectors sensitive in the (3.6-4.9) μm spectral range. The pitch is 10 μm. The acquisition frequency was set to 50 Hz. Observations were performed on two different scales using two different lenses.

Macroscale observations. The macroscale observations are obtained with a 50 mm lens (mounted with a 6 mm extension ring) yielding pixels of a size of approximately 50 μm. The integration time was set to 2200μs. The camera is usually used in full-frame mode leading to a resolution of 1920×1536 pixels. The built-in calibration was used for these measurements. The average NETD (Noise Equivalent Temperature Difference) was evaluated to be 32 mK.

Mesoscale observations. The mesoscale observations are obtained with a Mx1 lens decreasing the average pixel size to approximately 10 μm. The camera is used in quad-frame mode giving a resolution of 480×384 pixels. The integration time was set to 1800μs. An in-house pixelwise calibration is used for this type of measurements [25] reducing the average NETD to 8 mK.

All the presented experiments were performed at room temperature (measured around 25°C but not controlled). The specimen is placed inside a dark box and the experimental set-up is covered by dark sheets. The objective is to limit the influence of the environment on the measurements. When performing mesoscale observations, the specimen is covered by dark sheets and the use of the dark box is omitted as this setup causes minor vibrations of the infrared camera. Furthermore, the sample is usually covered with a high-emissivity black paint homogenizing the surface emissivity value between 0.98 and 0.985. Nevertheless, it should be mentioned that this practice is ignored when subsequent optical surface observations are needed as in the case presented in section 4.1.2 where microscope observations were carried out after each loading step. The emissivity range was evaluated using an HGH blackbody (model DCN 1000 N4) [26] via an indirect method involving the calculation of reflectance for two different temperatures chosen to be 15°C and 35°C (± 10°C with respect to the ambient temperature) [27]. In this case, the emissivity varies across the specimen surface between the values of 0.92 to 0.96. Consequently, the thermal measurements performed on an unpainted surface are slightly more dependent on external perturbations.

3 Analysis techniques

This section summarizes the techniques used for the identification of damage and dissipative mechanisms from experimental data obtained by infrared imaging. The first method addresses the compensation of the motion of the specimen submitted to mechanical loadings. This pre-processing of the experimental data ensures the local nature of measured temperature fields, which is one of the underlying assumptions of the subsequent pixelwise post-processing

techniques. Regarding the post-processing analyses, they include the generation of thermoelastic and dissipated energy fields, frequency analyses and the detection of thermal events. The generation of thermoelastic and dissipated energy fields is a commonly used method to describe the thermomechanical behaviour. Its applications to different kind of materials can be found in the literature [17, 18, 20, 22, 28, 29].

Frequency analyses are considered to be useful when dealing with metallic materials since they were shown to give access to the dissipated energy induced by plasticity [1, 21]. The last method has been developed for the sake of this study and aims at analysing the temperature singularities observed during cyclic loadings [23].

3.1 Motion compensation

3.1.1 State of the art

The thermodynamical framework used to express the dissipated energy $\Delta^\star$ and the thermoelastic coupling $\mathcal{C}_e$ (section 3.2) postulates that the state of each material point is given by a set of variables, called state variables. Therefore, the rigorous pixelwise identification of the dissipated energy and the thermoelastic coupling is not trivial since the underlying assumption states that each pixel corresponds to a given material point. As a matter of fact, this assumption is in general not valid because the tested sample deforms under the applied loading, whereas the camera is fixed [30]. This problem can be neglected if the undergoing strains remain limited so that the resulting displacements do not exceed the size of one pixel. However, if the undergoing strains become important, it might be convenient to compensate the deformations especially if the measured temperature fields are heterogeneous.

This can be done by transposing the temperature fields into the undeformed, reference configuration prior to their following analyses. However, this transposition requires the knowledge of the temperature and kinematic fields at the same time. Various experimental setups combining digital image correlation (DIC) and infrared thermography (IRT) can be found in the literature. If the tested specimens are thin enough to assume that the through-thickness gradients are negligible, the IRT and DIC measurements may be performed on the opposite faces of the sample [31, 32]. In order to measure the temperature as well as the displacement fields on the same surface, a dichroic mirror can be used in order to split the infrared and visual radiation to an infrared and CCD camera, respectively [33]. Another way of obtaining both temperature and displacement fields was proposed in [34]. This so-called infrared image correlation (IRIC) technique uses a high emissivity speckle to obtain simultaneously the deformation and temperature fields with the use of a single infrared camera. It should be noted that the implementation of all of these techniques is rather complex and their primary objective is to provide a rich experimental database that can be used to describe the thermomechanical properties of the tested

material. Nevertheless, the ability of the IRIC to compensate the displacements is specifically mentioned in [34]. The positive effect of the compensation of displacements on the results of temperature analyses was also demonstrated in [35]. A non-simultaneous two-step method combining digital image correlation with infrared measurements was used to improve the accuracy of the thermoelastic coupling fields and $2\times f$ lock-in component fields. When obtaining full-field kinematic measurements remains complicated, it might still be beneficial to use simpler compensation methods based upon the displacement of one or several markers. A compensation method based upon the displacements of various reflective spots was described in [30]. This method was shown to be able to track the temperature variation of material points of an elastomer subjected to large displacements. Another solution based exclusively on the displacement of one marker is presented in [36]. This study discusses the effect of this translational motion compensation on the evaluated thermoelastic coupling and dissipation fields. Even though these techniques do not provide full-field kinematic measurements, they may still produce a noticeable improvement of temperature analyses. Furthermore, their implementation is much simpler compared to full-field measurements.

Since the material used in this study is strongly heterogeneous, the implementation of a technique combining infrared thermography and digital image correlation would be complicated. Furthermore, the objective of the motion compensation, in our case, is to increase the accuracy of the temperature measurements rather than obtaining full kinematic fields. Thus, the motion compensation techniques used are based on methods presented in [30, 36] and rely on the displacements of high-emissivity markers.

3.1.2 Concept and illustration

As mentioned previously, the core of the motion compensation procedure used in this study lies in the detection of the displacements of one or two high-emissivity markers. As a first step, a sub-image containing only the marker and its closest vicinity has to be outlined. Then a reference sub-image capturing the position free of any mechanical loading has to be defined. Thereupon, a relative shift (computed with a sub-pixel precision) is calculated between the recorded sub-images and the reference one. This relative shift is calculated with the use of the masked normalized cross-correlation [37], available in the python package scikit-image [38]. It is appropriate to mention that even though the images recorded during the loading exhibit temperature changes, the proposed method succeeds in computing the correct shift and no prior histogram adjustments were found to be necessary. Two modifications of the final compensation procedure were developed depending on the observation scale.

1. Macroscale observations: The high-emissivity markers are located outside the region of interest (ROI). By evaluating the displacements of these markers, it is possible to compensate the translation motion of the ROI as well as the average dilatation (contraction) of its original height. Furthermore,

these height dilatations (contractions) can be interpreted as a measure of the average longitudinal deformation (figure 3 and figure 4). This quantity may thus provide information on the mechanical behaviour, *e.g.* the evolution of the residual deformation (figure 4). The increase in accuracy of the subsequent post-processing is demonstrated in section 3.2.2.

2. Mesoscale observations: Since the size of the observed area is significantly reduced with respect to the macroscale observations, only one marker (figure 27) is used limiting the motion compensation to translation only. Nevertheless, this practice still leads to a sufficient accuracy gain because the displacements induced over the observed area by the sample deformation remain negligible.

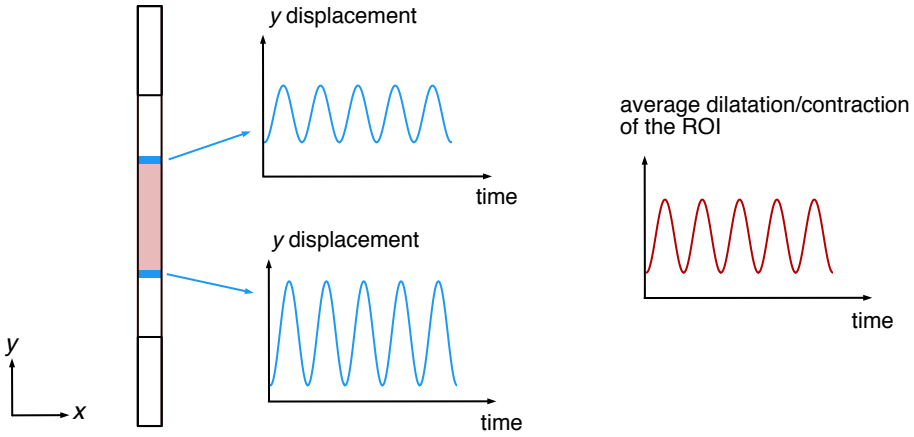

Fig. 3 Illustration of the motion compensation technique used for macroscale observations.

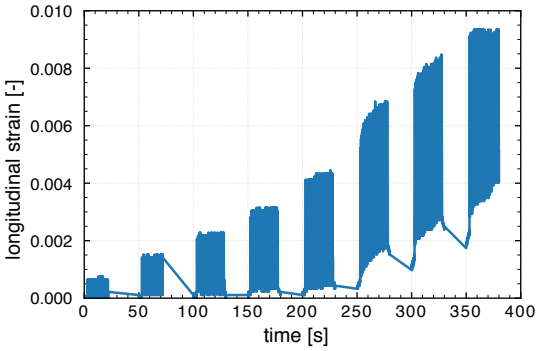

Fig. 4 Illustration of the longitudinal strain computed from marker displacements during a heat build-up experiment.

The effect of the macroscale compensation technique is illustrated in figure 5. This figure plots the temperature difference fields measured on the face

of a specimen experiencing cyclic loadings. The temperature difference was obtained by subtracting the temperature field measured during the peak load of the 2nd cycle from the temperature field measured at the end of the same cycle. The fields were evaluated with (figure 5-(b)) and without motion compensation (figure 5-(a)). It is possible to notice that the perturbations induced by specimen displacements are visible only in the non-compensated field. The compensation effect is obvious especially in the proximity of the bottom marker, where the induced displacements are the most significant.

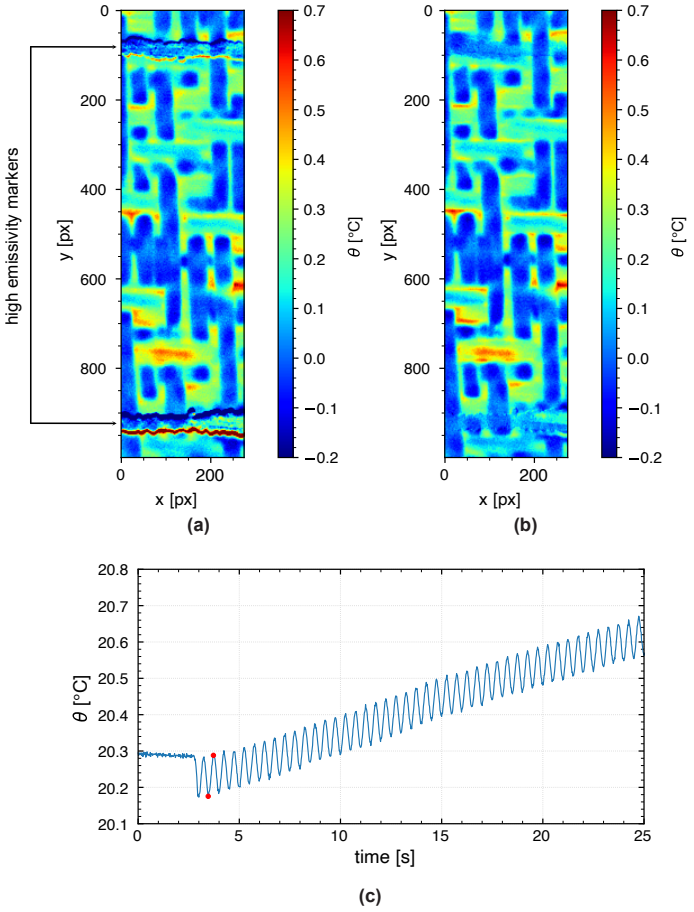

Fig. 5 Illustration of the motion compensation effect. (a) temperature difference field obtained without motion compensation, (b) with motion compensation and (c) average temperature evolution.

3.1.3 Validation

In order to validate that the ROI dilatations/contractions can be used as a measure of longitudinal deformation, infrared imaging was employed simultaneously with digital image correlation (DIC) for several tests as illustrated in figure 6. The infrared camera was used for side face observations while the CCD camera was pointed towards the front face. Since the acquisition frequency of the CCD camera was limited to 2Hz, the loading frequency was set to 0.2 Hz in order to obtain a sufficient number of images throughout the complete mechanical cycle. The longitudinal deformation was then calculated as the average over the region of interest (60×14mm located on the front face of the specimen). The obtained results are summarized in figure 7. The deformation obtained with infrared marker detection correlates well with the one computed by digital image correlation. Figure 8 shows that the difference does not exceed 0.0007 which is relatively low compared to the absolute values of deformation, given by the two techniques (10 times lower than the maximum absolute value). Therefore, the accuracy of the marker detection technique can be concluded satisfactory.

Fig. 6 Experimental setup combining infrared imaging with digital image correlation.

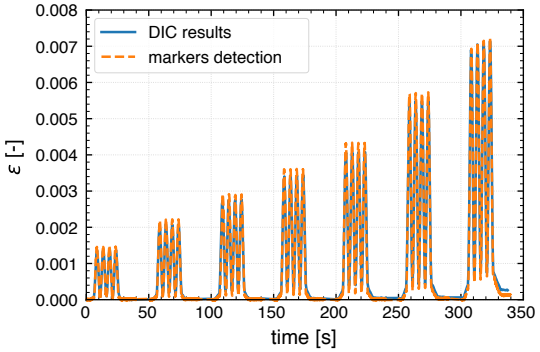

Fig. 7 Comparison of the average longitudinal deformation computed by marker detection and DIC.

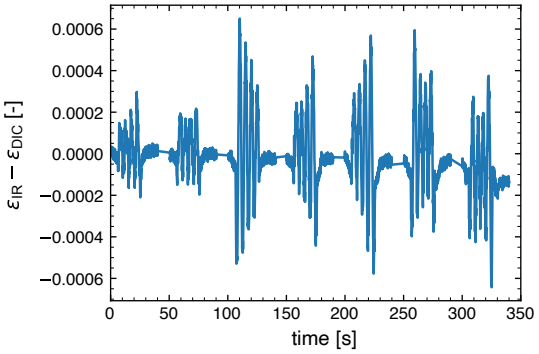

Fig. 8 Difference between the average longitudinal deformation computed by marker detection and DIC.

3.2 Dissipated energy and thermoelastic coupling fields

3.2.1 Concept and bibliography

Even though the temperature fields contain valuable information, further post-processing is required if intrinsic characteristics of the material need to be obtained. Heat build-up analyses usually necessitate retrieving the heat sources responsible for the measured temperature variations. This section provides a description of this procedure.

In this study, an adiabatic approach was chosen to retrieve the heat sources responsible for temperature variations [17, 18, 22, 39]. This technique has been shown to provide access to the dissipated energy and thermoelastic coupling fields. As mentioned in [23], a reduced amount of cycles limits the damage accumulation during the experiment. The experimental evaluation of the dissipated energy is based on the heat equation presented in [1, 17]. Its simplified form can be written as

$$\rho c_p \left.\frac{\partial \theta}{\partial t}\right|_{t\to 0} = f\Delta^\star + \mathcal{C}_e \tag{1}$$

with θ the temperature variation (the difference between the instantaneous and initial temperature $T - T_0$), f the mechanical frequency, $\Delta^\star$ the cyclic dissipated energy and $\mathcal{C}_e$ the thermo-elastic coupling contribution. The material parameters needed for the solution are the specific mass ρ and the specific heat c_p. When the applied loading is cyclic and of a sinusoidal form, the solution of the simplified heat equation is

$$\forall t \in \mathbb{R}_+, \theta(t) = \frac{f}{\rho c_p}\Delta^* t + \mathcal{C}_e \sin\left(2\pi f t + \phi\right) \tag{2}$$

The variable ϕ represents the phase shift between the thermal and mechanical loading signal. The pixelwise post-processing technique used in this study is presented in [22]. The key idea is to perform the identification using equation

2 for every pixel of the region of interest. This allows generating the respective thermoelastic and dissipated energy fields. The reader can refer to [23] for a more detailed verification of the underlying hypotheses of the adiabatic approach (adiabaticity, mechanical hysteresis stabilization).

As equation 2 states, in order to plot a dissipated energy map from the identified temperature growth, the values of the specific mass ρ and the specific heat c_p have to be provided. For the sake of simplicity, the identified slope $\frac{\partial \theta}{\partial t}|_{t\to 0}$ (°C/s) is multiplied by a weighted average product of the material parameters, $\overline{\rho \cdot c_p}$. The effective value of the product of the specific mass $\bar{\rho}$ and the specific heat $\bar{c}_p$ is calculated using the fibre V_f and matrix V_m volume ratios as follows:

$$\overline{\rho \cdot c_p} = V_f \cdot \rho_f \cdot c_{p,f} + V_m \cdot \rho_m \cdot c_{p,m} \tag{3}$$

where ρ_f, $c_{p,f}$ and ρ_m, $c_{p,m}$ are respectively the properties of the fibres and the matrix. It should be noted that a pixelwise attribution remains possible. Nevertheless this approach was found to give similar results, as the products $\rho_m \cdot c_{p,m}$ and $\rho_f \cdot c_{p,f}$, calculated for each component separately, differ by less than 20%.

3.2.2 Illustration

Figures 9 and 10 give an example of a thermoelastic coupling and dissipated energy fields and illustrate the effect of the motion compensation. In order to emphasize the influence of the undergoing displacement, the areas containing the signature of the two high-emissivity markers were not cropped. By comparing the two figures, it becomes clear that while the dissipated energy maps resemble closely, the thermoelastic coupling maps exhibit obvious differences. The increased sensitivity of the thermoelastic coupling component was expected since the latter varies at the rate of 2 Hz while the value of the dissipated energy represents an average elevation over the whole identification interval and therefore tends to be locally smoothed out by diffusion. In order to quantify the effect of the motion compensation, the identification residuals were computed according to the following equation

$$\text{res} = \sum_{i=1}^{N} \left| \theta_i^{\text{exp}} - \theta_i^{\text{calc}}\left(t_i\right) \right| \tag{4}$$

The variable θ_i^{exp} represents the temperature variation measured at time t_i, θ_i^{calc} is the value computed at time t_i according to the equation 2. The residuals are calculated for all pixels of the ROI and the results are plotted in the form of histograms in figure 11. The positive effect of the motion compensation technique is obvious as it can be seen that the residuals diminish when the motion compensation is used.

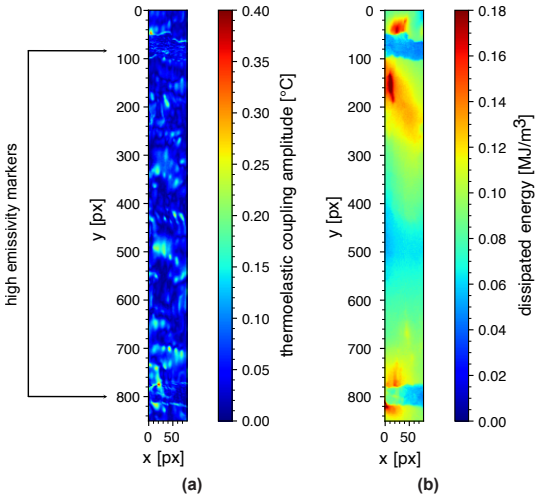

Fig. 9 Illustration of infrared imaging results obtained for the normalized stress amplitude of 7.6 MPa/MPa using the macroscale technique of motion compensation: (a) thermoelastic coupling map, (b) dissipated energy map.

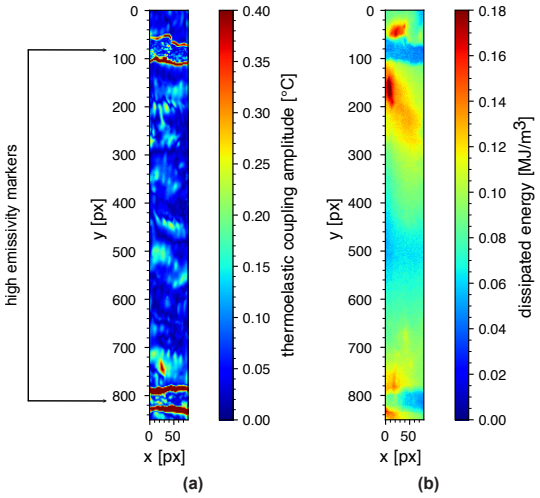

Fig. 10 Illustration of infrared imaging results obtained for the normalized stress amplitude of 7.6 MPa/MPa using no technique of motion compensation: (a) thermoelastic coupling map, (b) dissipated energy map.

3.3 Thermal events

3.3.1 Concept

This section focuses on thermal events that were described in [23] as local irregularities occurring during the loading period. An illustration of such an event is presented in figure 12. Before describing the detection protocols, it is useful to recall the characteristic features of these events. As stated in [23],

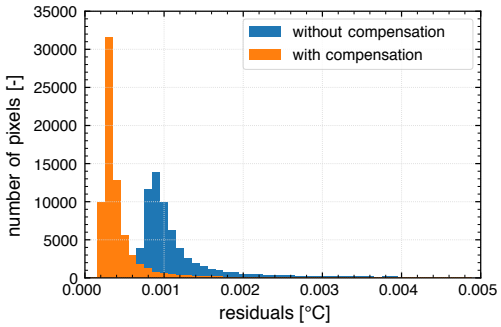

Fig. 11 Residual histograms obtained with and without motion compensation.

these thermal events include a steep increase of the temperature variation, nevertheless the affected area remains relatively small. Furthermore, the duration of these abrupt irregularities is limited to a few milliseconds before the temperature increase is diffused and the affected zone returns to a dynamic thermal equilibrium. It was also systematically observed that the occurrence of a thermal event induces a decrease in the thermoelastic coupling contribution (as illustrated in figure 12-(a)). Two dedicated detection protocols were

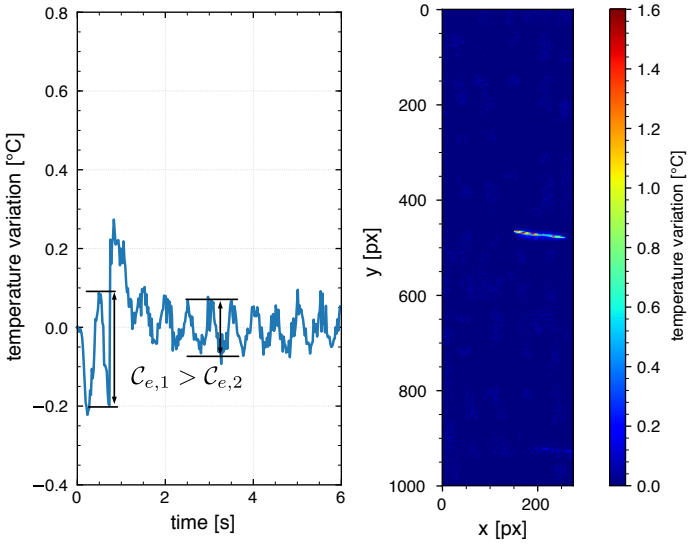

Fig. 12 Thermal event illustration: (a) evolution of the temperature variation of a specific pixel [200,475], (b) temperature variation map for a specific frame.

developed in order to detect the regions affected by thermal events. The first one applies a thresholding algorithm in order to identify the pixels exhibiting a significant increase in temperature; the second one makes use of the decrease

in the thermoelastic coupling contribution. The two procedures will be illustrated on a specimen observed on the front face and tested with a classic heat build-up protocol (figure 13).

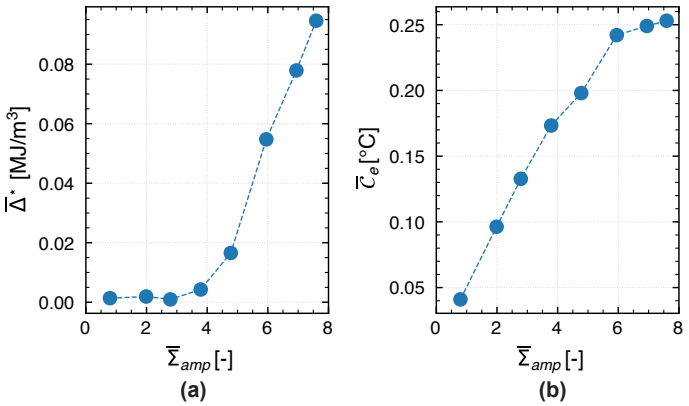

Fig. 13 Macroscale average results of the specimen used for the illustration of the thermal events detection techniques: (a) heat build-up curve, (b) amplitude of the thermoelastic coupling contribution.

3.3.2 Thresholding detection technique

The thresholding detection technique makes use of the local temperature increases. The key idea is to identify all the pixels whose temperature exceeds a given threshold between two successive images. The threshold value has, therefore, a paramount influence on the obtained results. If the fixed value is too small, the algorithm might detect pixels that are not linked to any event, especially when the applied loading is relatively high and the overall temperature elevation is significant (figure A1). On the other hand, if the applied threshold is too high, events exhibiting lower temperature increases will be missed. It needs to be emphasized, that the time difference corresponding to two successive images equals to 0.02 s, as the acquisition frequency was set to 50 Hz and was kept constant during the entire campaign. Considering this acquisition frequency and the investigated material, the threshold value was set to 0.3 °C. The determined value is based on sensitivity studies and the description of the mesoscale cooling process presented in the Appendix A.

Figure 14 illustrates the results obtained for the normalized stress amplitude of 3.8 MPa/MPa in the form of a binary map. Five distinct regions were detected. All the regions have a form of long elongated ellipses and are horizontally oriented.

3.3.3 Thermoelastic coupling detection technique

The thermoelastic coupling contribution is, under some assumptions [40], proportional to the local stress state. It is therefore reasonable to assume that as

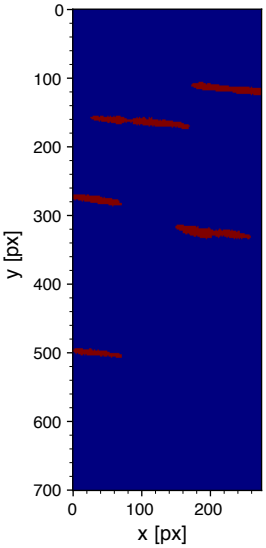

Fig. 14 Thresholding detection results obtained for the normalized stress amplitude of 3.8 MPa/MPa.

long as the material behaviour remains mostly elastic, the thermoelastic coupling amplitude identified during each loading step will remain proportional to the applied average stress. At macroscale level, this initial linearity can be observed when analysing the thermoelastic coupling curve (figure 13-(b)). This linearity is exploited during the detection procedure. At least two thermoelastic maps have to be provided in order to detect the events occurring between their respective time windows. For the purpose of demonstration, the third and the fourth loading block will be used in the following example. The detection procedure can be described in three steps (two of which are illustrated in figure 15):

1. The thermoelastic coupling map obtained for the third block at 2.8 MPa/MPa is taken as a reference. In order to obtain the theoretical coupling map of the fourth block corresponding to 3.8 MPa/MPa, each pixel is multiplied with the ratio $\sigma_{\max 4}/\sigma_{\max 3} = 3.8/2.8$ (figure 15-(a)).
2. In order to highlight the appearing irregularities, the theoretical coupling map is subtracted from the one obtained experimentally. Two regions appear in the resulting difference map (figure 15-(b)).
3. The last step consists in segmenting the two distinct regions. Multiple methods of object segmentation exist, the results shown in this article used the random walker algorithm [41], available in the scikit-image package [38]. Nevertheless, it should be noted that other methods of segmentation might be suitable for this purpose.

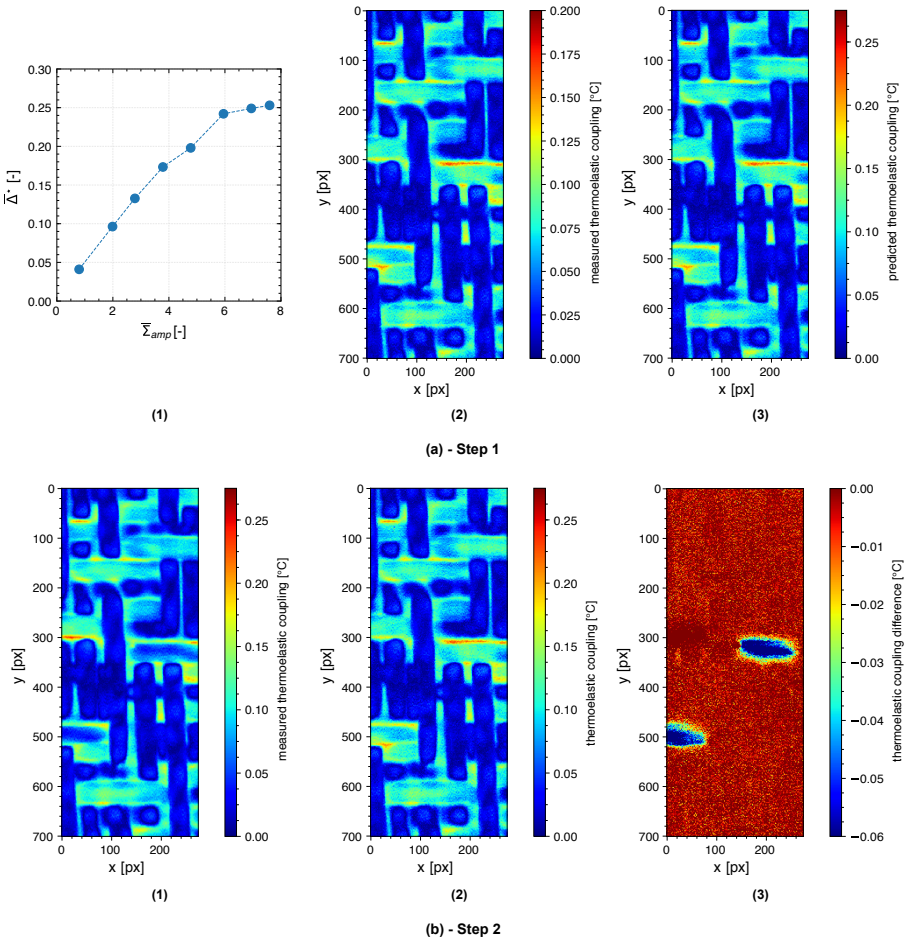

Fig. 15 Illustration of the thermoelastic coupling detection process.

The detection results are presented in the form of a binary map (figure 16). It is possible to highlight two regions affected by the occurrence of thermal events. The regions are ellipsoidal and horizontally oriented. Regarding the detection interval, it should be emphasized that the latter is naturally limited by the respective identification intervals chosen for the evaluation of the thermoelastic coupling maps, *i.e.*, the two thermal events identified in the case presented above occurred after the end of the third and before the end of the fourth identification interval.

3.4 Frequency analyses

3.4.1 Concept and bibliography

This section presents the extension of the evaluation of the experimental maps to frequency analyses. Time-frequency analyses often call the attention to the

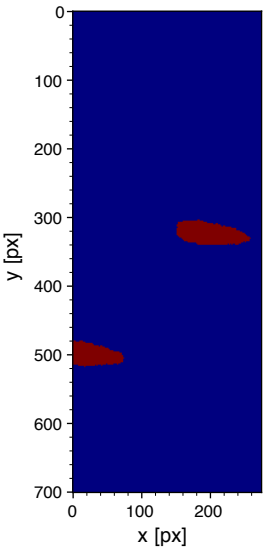

Fig. 16 Illustration of results of the thermoelastic coupling detection process.

signal intensity at 2×f, as the latter can be useful in describing the thermomechanical behaviour of the studied material. This component has been assumed to give access to the dissipated energy under cyclic loadings in the case of metallic materials [21, 36, 42]. Regarding the woven composites, this 2×f component is considered to highlight the areas with high intensity of friction providing from relative movements of crack faces [23]. Therefore, this phenomenon can only be observed when cracks have been induced in the material as a result of the applied loading.

3.4.2 Generation of 2×f intensity maps

As presented in [23], when analysing the thermomechanical behaviour of woven composites, it is useful to extend the pixelwise post-processing routine to frequency analyses. The procedure is illustrated using a classic heat build-up experiment, specifically its last loading step (figure 17). For the sake of correct interpretation of the following analyses, it is important to specify that the loading frequency was set equal to 2Hz throughout the whole experiment. After the application of the motion compensation, the temperature evolution of each pixel is analysed over the identification interval (0-3s) and can be regarded as a signal. This signal can then be transformed into the frequency domain using the discrete Fourier transform. The sampling frequency of the signal corresponds to the acquisition frequency of the IR camera (in this case equal to 50 Hz). The transformation allows plotting the amplitude spectrum for each pixel and, thus, analysing the relative importance of different amplitude components. The results are shown in figure 18.

Two different pixels located in the ROI are analysed. Their respective temperature variations, measured during the identification interval, are plotted in

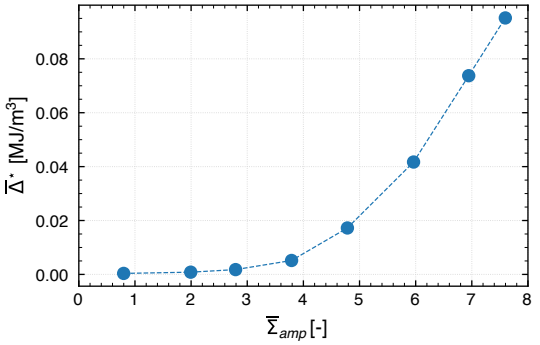

Fig. 17 Heat build-up curve of the specimen used for the illustration of 2×f intensity maps.

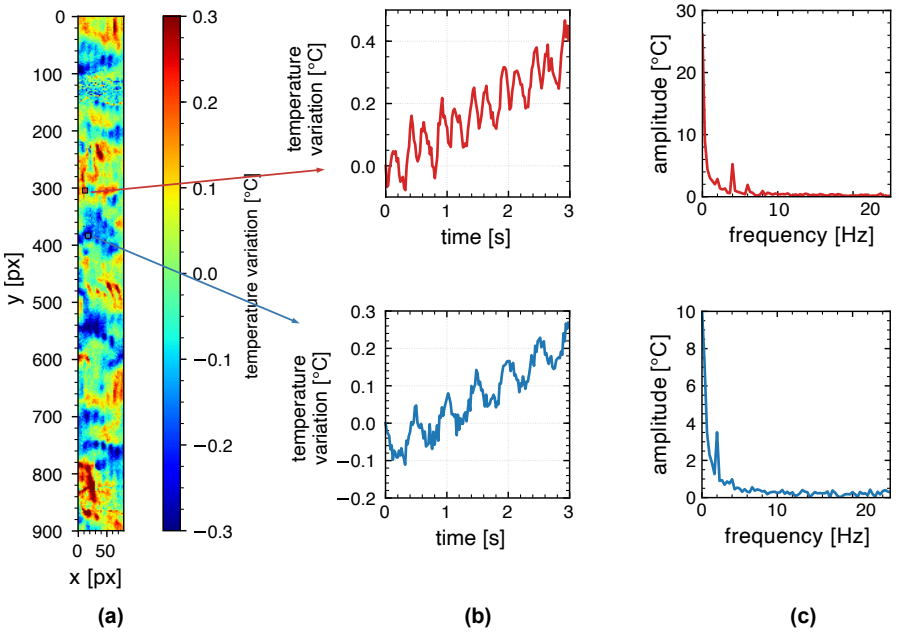

Fig. 18 Illustration of the temperature variation obtained for the normalized amplitude of 7.6 MPa/MPa of a classic heat build-up experiment: (a) temperature variation map at 0.22 seconds, (b) temperature variations of two pixels located in the ROI, (c) the amplitude spectra of two pixels located in the ROI.

figure 18-(b). It is obvious that the temperature of the pixel 1 varies more rapidly than the one of pixel 2. This is naturally reflected in the amplitude spectra of these two pixels shown in figure 18-(c). The lower amplitude spectrum shows two distinct peaks. The first and the most important peak occurs at 0 Hz and corresponds to the average of the temperature variation measured over the temporal window. The second peak occurs at 2 Hz and corresponds to the thermoelastic coupling contribution. Since the thermoelastic coupling contribution is a function of the local stress state, it varies simultaneously with

respect to the applied loading, in this case at the rate of 2 Hz. By analysing the upper amplitude spectrum, it is possible to notice that the most significant amplitude peak occurs at 4 Hz corresponding to the double of the loading frequency, $2 \times f$. In order to obtain a full-field overview, the $2 \times f$ amplitudes are computed for all pixels of the ROI. The results are then plotted in the same way as in the case of the thermoelastic coupling fields or dissipation fields (figure 19).

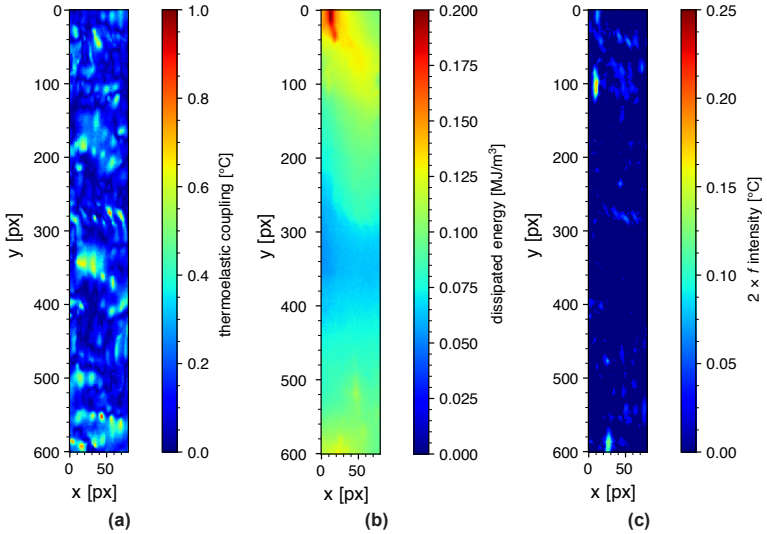

Fig. 19 Infrared imaging results obtained for the normalized stress amplitude of 7.6 MPa/MPa : (a) thermoelastic coupling map, (b) dissipated energy map, (c) 2xf intensity map.

4 Discussion

4.1 Thermal events

4.1.1 Critical comparison of the detection methods

In order to discuss the performance of the two detection techniques, the events obtained during different steps of the presented heat build-up experiment (figure 13) were plotted in figure 20 and in figure 21. The results are plotted in a cumulative way, *i.e.* each map highlights the zones detected up to the given loading block. It is possible to notice that the events do not necessarily appear at the same block. Nevertheless, this finding is plausible since the time windows are different for the two techniques. Globally, it is possible to state a conclusive correlation until the applied amplitude reaches 6 MPa/MPa. After exceeding this value, the obtained results start to differ slightly. The shape of

the detected areas is analogous, yet, due to diffusion effects, the thermoelastic detection technique systematically overestimated the detected surface area.

The advantage of the thermoelastic coupling technique lies in its efficiency, as it does not require analysing all the recorded images. Furthermore, since this technique does not analyse the temperature variations, it is able to detect even low intensity events that induce temperature elevations lower than 0.3°C. Yet, an accurate detection requires the use of a motion compensation technique ensuring the correct overlapping of the coupling maps used at the input. The thresholding detection technique represents a more time-consuming but

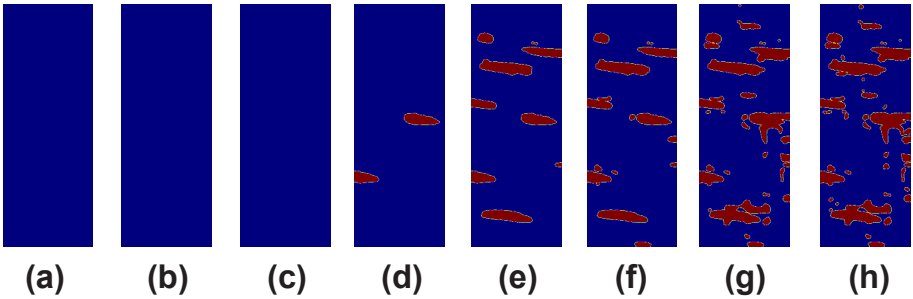

Fig. 20 Cumulative thermoelastic coupling detection results obtained during different loading steps corresponding to the stress amplitudes of: (a) 0.8 MPa/MPa, (b) 2 MPa/MPa, (c) 2.8 MPa/MPa, (d) 3.8 MPa/MPa, (e) 4.8 MPa/MPa, (f) 6 MPa/MPa, (g) 7 MPa/MPa, (h) 7.6 MPa/MPa.

a robust way to identify thermal events. Since the identification is done over a shorter time interval (0.02s), the blur coming from diffusion remains negligible. This allows a more accurate description of the shape associated to thermal events. Yet, as mentioned in section 3.3.2, the results are entirely dependent on the thresholding value that may vary according to the experimental conditions (tested material, loading type, acquisition frequency etc.).

After having discussed the pros and cons of the two techniques, it is possible to conclude that in order to minimize the detection error, they should be used simultaneously as illustrated in the following section.

4.1.2 Link to microstructure observations

In order to confirm that the thermal events are linked to crack formation, multiple observations, focusing on both front faces and side faces, were carried out on different unpainted specimen. These observations investigated the areas highlighted by the detection protocols and it was systematically confirmed that thermal events are associated with the creation of local damage. In order to illustrate this phenomenon, a posteriori side face observations are displayed in figures 23 and 24. The investigated specimen was tested with a classic heat build-up protocol (figure 22). The lower quality of the experimental data is mostly due to a heterogeneous emissivity of the observed surface since

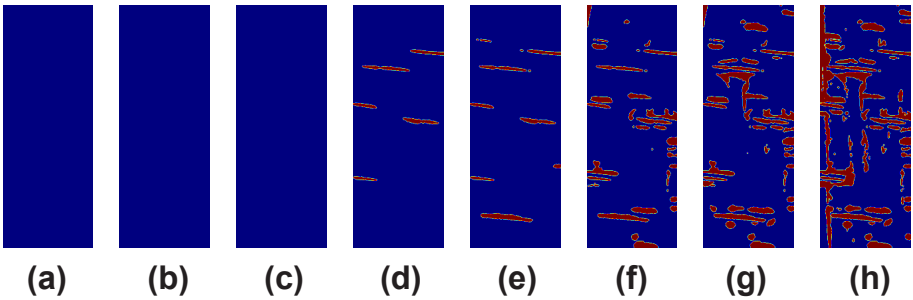

Fig. 21 Cumulative thresholding detection results obtained during different loading steps corresponding to the stress amplitudes of : (a) 0.8 MPa/MPa, (b) 2 MPa/MPa, (c) 2.8 MPa/MPa, (d) 3.8 MPa/MPa, (e) 4.8 MPa/MPa, (f) 6 MPa/MPa, (g) 7 MPa/MPa, (h) 7.6 MPa/MPa.

the specimen was not painted (section 2.3). Nevertheless, the event detection techniques are still applicable.

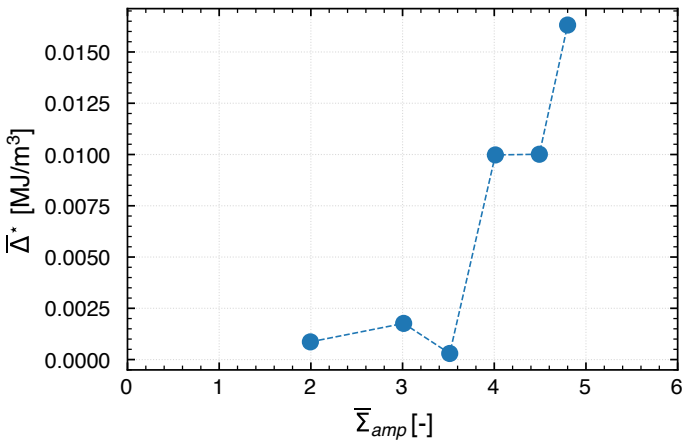

Fig. 22 Heat build-up curve of the specimen used for a posteriori observations of thermal events.

Figure 23 presents the results obtained during the second loading step for the normalized stress amplitude of 3 MPa/MPa. The microscope observations of the two highlighted regions confirmed the presence of cracks. It should be pointed out that the thermal events were detected uniquely with the thermoelastic coupling protocol. Indeed, it was verified that these events induce temperature elevations inferior to the fixed threshold of 0.3°C. Consequently, these two techniques should be considered complementary rather than competing and their simultaneous use should be systematic. Figure 24 presents the cumulative results obtained until the fourth loading step at 4 MPa/MPa. In this case, both techniques give the same results. The surface observations reveal an apparent development of damage confirming, again, the link between thermal events detected and the formation of cracks.

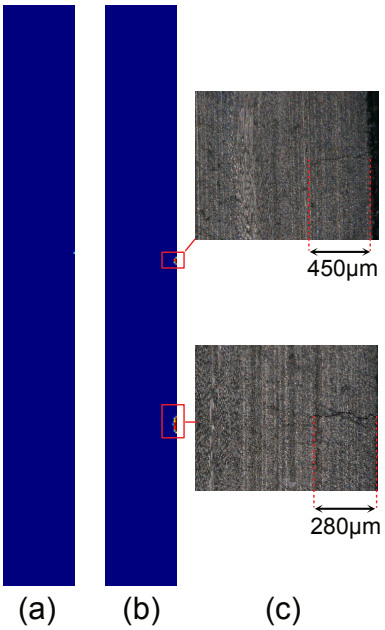

Fig. 23 Microscope observations of thermal events for the normalized stress amplitude of 3 MPa/MPa: (a) thresholding detection results, (b) thermoelastic coupling detection results, (c) cracks observed.

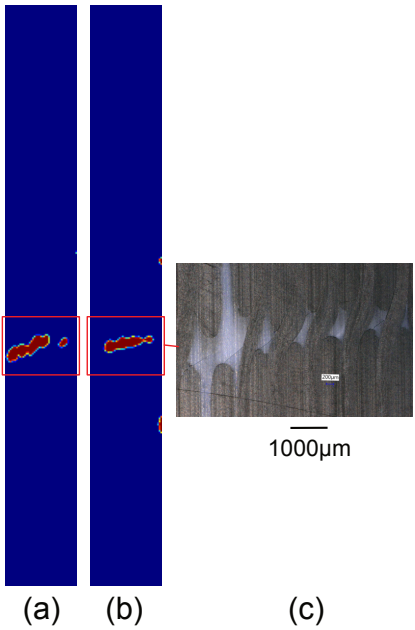

Fig. 24 Microscope observations of thermal events for the normalized stress amplitude of 4 MPa/MPa: (a) thresholding detection results, (b) thermoelastic coupling detection results, (c) cracks observed.

4.2 Frequency analyses

4.2.1 Link to friction detection

When examining figure 19-(c), it is possible to notice two zones of increased $2\times f$ intensity that would, according to [23], indicate an increased importance of friction. However, in order to support this hypothesis, it would be appropriate to carry out surface observations of these two zones that would confirm the presence of cracks. Furthermore, it would be useful to zoom on the investigated areas when loading is applied and check for the relative movements that could lead to the assumed friction. Nevertheless, these observations cannot be carried out if the specimen is painted black and will therefore be demonstrated on a different unpainted specimen.

4.2.2 Application to a reverse heat build-up experiment

Reverse heat build-up experiments proved to be particularly convenient for the investigation of the damage-related friction as the majority of cracks are introduced during the initial loading step. The effects induced by cracks can then be analyzed during the subsequent loading steps when almost no further

cracking occurs. After the experiment, the observed surface was inspected with a microscope.

The global reverse heat build-up curve is displayed in figure 25. Figure 26 shows the experimental maps obtained during the second loading step.

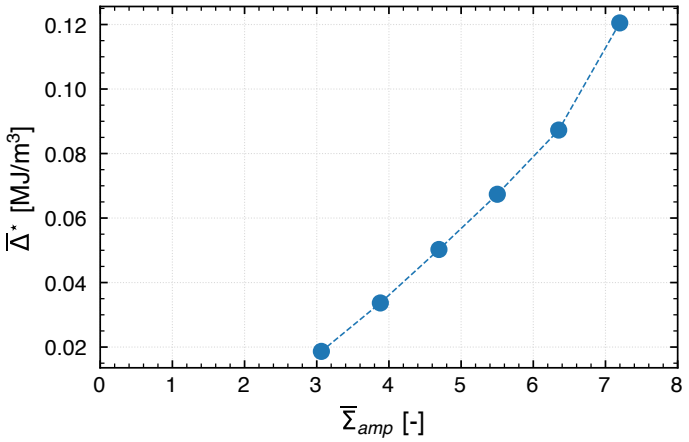

Fig. 25 Reverse heat build-up curve.

The 2×f intensity map reveals an increase in the detected 2×f amplitudes in the upper right corner highlighted by the red box. The microscope observation of the corresponding zone confirmed the presence of multiple cracks that could lead to friction (figure 27).

In order to study the damage kinematics, infrared observations under cyclic loadings, using the M×1 objective (section 2.3), were conducted after the reverse heat build-up experiment. Figure 28 summarizes six images obtained during one loading cycle. The rigid body motion was compensated using the marker located in the upper left corner (figure 27-(c)). By observing the images presented in figure 28, a relative movement between the yarn of interest and its surroundings can be noticed. Furthermore, a relative movement occurring under the applied loading was noticed inside the examined yarn. In order to confirm the importance of the $2\times f$ component, the temperature evolution of one pixel located in the affected zone (figure 27-(c)) is shown in figure 29. This figure shows clearly that during one mechanical cycle, the temperature increases and decreases twice. This observation can be explained by friction that occurs during the loading and unloading phase and causes rapid elevations of the temperature that are immediately diffused.

Conclusions

This article illustrates the use of 4 post-processing techniques applied to a layer-to-layer woven composite. The importance of the motion compensation procedure was illustrated during the evaluation of thermoelastic and

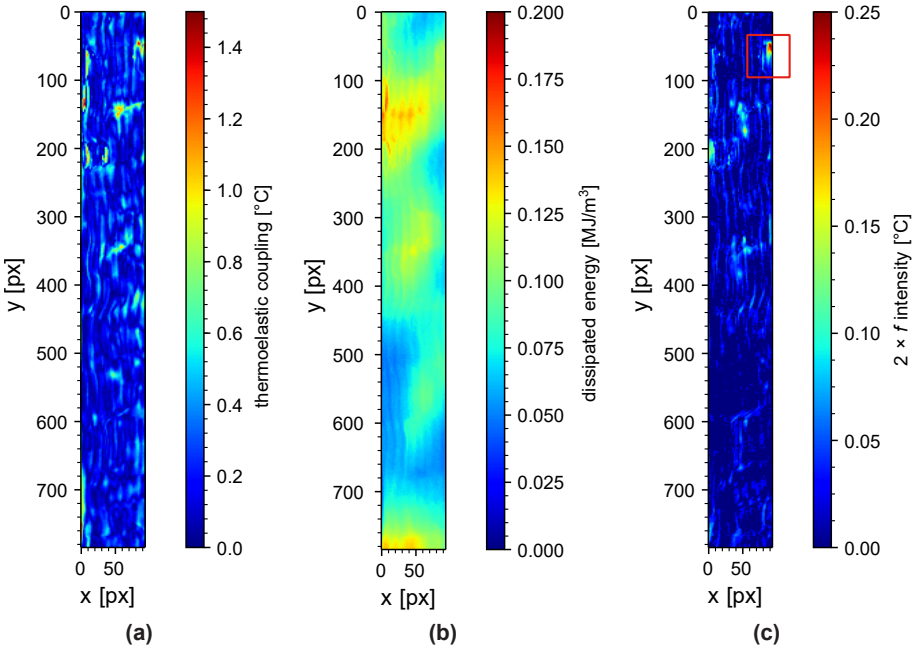

Fig. 26 Infrared imaging results obtained for the normalized stress amplitude of 6.35 MPa/MPa : (a) thermoelastic coupling map, (b) dissipated energy map, (c) 2xf intensity map.

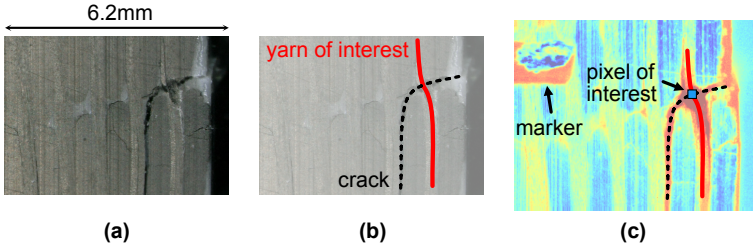

Fig. 27 Microscope observation of a zone exhibiting an increased 2xf intensity: (a) microscope observation, (b) highlighting of the investigated features, (c) - IR observation of the investigated zone.

dissipation fields. Indeed, the use of this pre-processing method proved to decrease the identification residuals and revealed to be particularly important when analysing the thermoelastic coupling contribution. The following post-processing technique presented in this article aims at detecting thermal events occurring when the specimen is being subjected to loading. Two versions of this detection technique were presented. It was concluded that these two techniques are complementary and should be systematically used at the same time as this practice seems to limit the risk of missing certain events. Microscope observations confirmed that the thermal events detected are associated with the creation of cracks. The fourth post-processing technique focuses on the $2\times$f

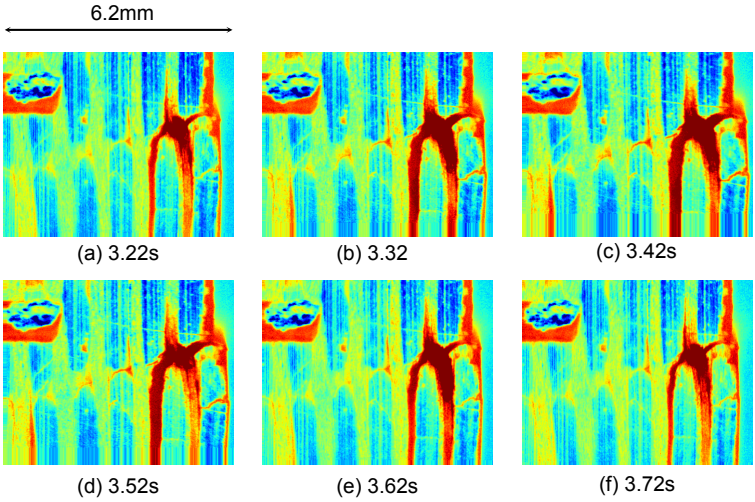

Fig. 28 Mesoscopic observations of a zone exhibiting a high $2 \times f$ intensity.

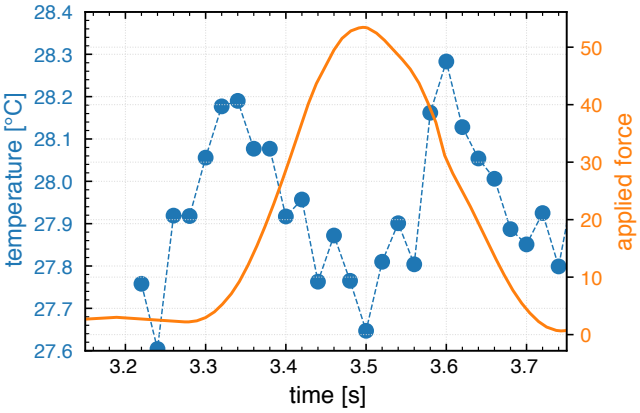

Fig. 29 Temperature evolution of a pixel located in the damaged zone.

amplitude component that is considered to highlight areas with an increased contribution of friction. Further observations of one of those areas confirmed consistently the presence of damage. Moreover, it was confirmed that relative movements between the damaged regions occur when the specimen is loaded supporting thus the friction explanation theory.

Acknowledgments. The research presented in this article was funded by the Safran Group, France. Safran Tech-Composites Platform is acknowledged for the manufacturing of the samples used in this study. The authors would also like to thank the French ANRT Agency for its financial support (CIFRE n°2017/1456).

Declarations

Some journals require declarations to be submitted in a standardised format. Please check the Instructions for Authors of the journal to which you are submitting to see if you need to complete this section. If yes, your manuscript must contain the following sections under the heading 'Declarations':

- Funding
- Conflict of interest/Competing interests (check journal-specific guidelines for which heading to use)
- Ethics approval
- Consent to participate
- Consent for publication
- Availability of data and materials
- Code availability
- Authors' contributions

If any of the sections are not relevant to your manuscript, please include the heading and write 'Not applicable' for that section.

Appendix A Threshold value evaluation

As mentioned in section 3.3.2, the results of the thresholding detection technique are strongly dependent on the fixed thresholding value. The overall objective is to set the thresholding value as low as possible in order to detect even low energy events that do not lead to high temperature elevations. However, there are two major constraints. The first limitation is avoiding the detection of regions exhibiting significant temperature increases that are not caused by thermal events. This concerns particularly high stress amplitudes that might induce temperature elevations exceeding the fixed threshold. The second challenge is limiting the diffusion-affected area. Indeed, when a thermal event occurs, it produces a temperature elevation that is rapidly diffused. This leads to a temperature elevation in the vicinity of the event that might also exceed the given threshold. However, as this excess is not linked to a formation of a new event but rather to the propagation of the original one, this affected area should not be included in the detection results. In order to verify these two aspects that might skew the detection results, a sensitivity study and mesoscale cooling observations were carried out.

The results of the sensitivity study presented in figure A1 were obtained on a specimen observed on a front face and tested with a classic heat build-up protocol (figure 13). Two variables were analysed: the number of events detected and their relative surface. The plot displays the results obtained for the entire heat build-up test for different thresholding values that vary from 0.05 to 0.5. Even though, the detected relative surface seems to stabilize at the value of 0.2 °C, the number of the detected events seems to stabilize between the values of 0.3 and 0.4. Since it is the relative surface that is more often

used for further analyses and since the difference between the events counted at 0.3, and 0.4 °C is not critical, the thresholding value was set to 0.3 °C.

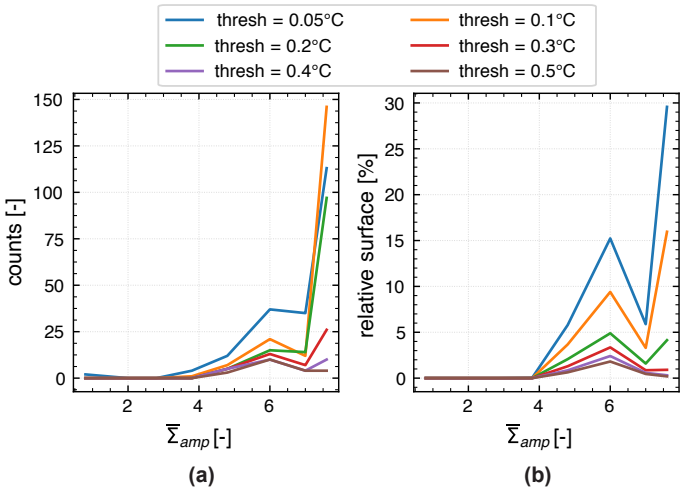

Fig. A1 An example of the sensitivity of the results on the thresholding value.

In order to describe the diffusion effects at the mesoscale level, observations of the cooling period that follows the creation of a thermal event were carried out. The idea is to apply a sharp mechanical loading followed by a creep test that generates a thermal event that can be observed with an infrared camera. These observations are then used to quantify the diffusion rate (figure A2).

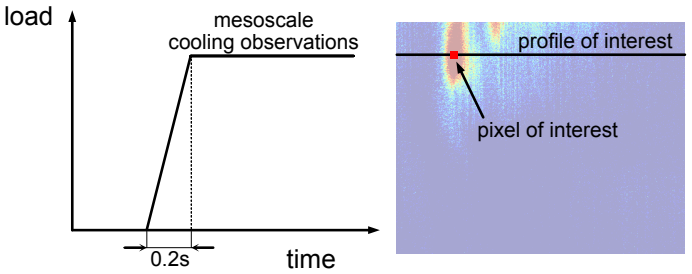

Fig. A2 Illustration of the creep test.

The cooling period is schematically depicted in figure A3. It is possible to notice that the initial temperature elevation diffuses rapidly. Figure A4 confirms that a pixel localized in the middle of the affected area takes less than one second to reach thermal equilibrium.

Furthermore, it is possible to notice that the thermally affected area remains relatively small as the initial temperature increase does not tend to spread in the observed x-y plane. This is confirmed by figure A4 that shows

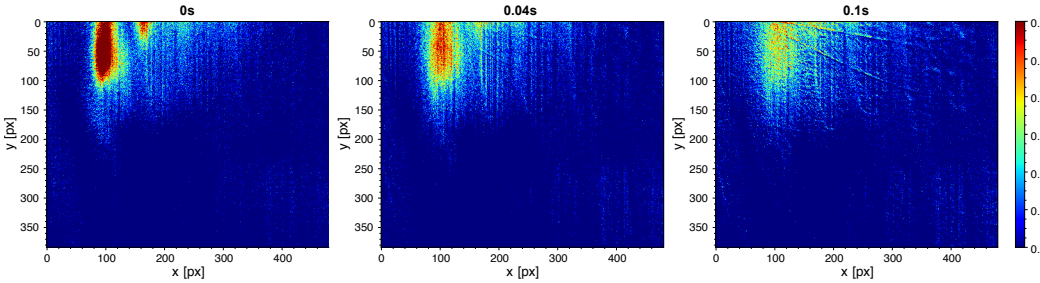

Fig. A3 Illustration of the cooling period following the development of a thermal event.

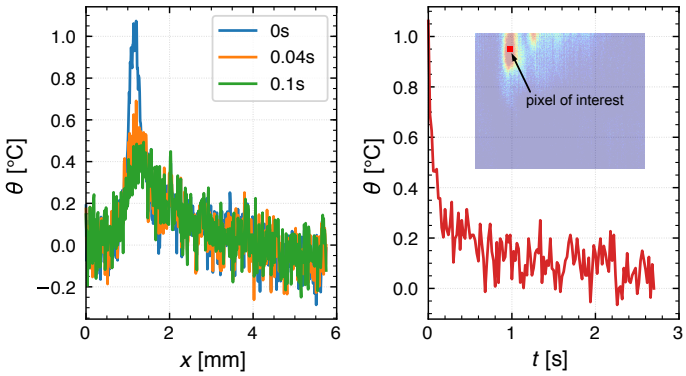

Fig. A4 Illustration of temperature profiles obtained in the ROI during the cooling period.

the evolution of a temperature profile obtained along the x-direction. It is evident that the change in the width of the initial profile remains unimportant, especially at the macroscale level at which the detection process is normally realized. This would mean that the heat diffusion happens primarily in the direction that is perpendicular to the observed x-y plane.

Even though these afore-presented analyses are not exhaustive, they may serve as a rule of thumb when a thresholding value needs to be determined for a different material. The identified value of 0.3°C seems to detect the majority of the produced events without skewing the results with falsely identified pixels. Furthermore, the errors induced by diffusion effects were shown to be negligible.

References

[1] Chrysochoos, A., Louche, H.: An infrared image processing to analyse the calorific effects accompanying strain localisation. International Journal of Engineering Science **38**, 1759–1788 (2000)

[2] Chrysochoos, A.: Thermomechanical analysis of the cyclic behavior of materials. Procedia IUTAM **4**, 15–26 (2012)

[3] Kordatos, E.Z., Aggelis, D.G., Dassios, K.G., Matikas, T.E.: In-situ monitoring of damage evolution in glass matrix composites during cyclic loading using nondestructive techniques. Applied Composite Materials **20**, 961–973 (2013)

[4] Weber, W.: Über die spezifische Wärme fester Körper insbesondere der Metalle. Annalen der Physik und Chemie **96**, 177–213 (1830)

[5] Thomson, W.: On dynamical theory of heat. Transactions of the Royal Society of Edinburgh, 261–283 (1853)

[6] Sharpe, W.N.: Springer Handbook of Experimental Solid Mechanics, (2008)

[7] Germain, P., Nguyen, Q.S., Suquet, P.: Continuum thermodynamics. Journal of Applied Mechanics, Transactions ASME **50**(4), 1010–1020 (1983)

[8] Ding, Y.Q., Yan, Y., McIlhagger, R., Brown, D.: Comparison of the fatigue behaviour of 2-d and 3-d woven fabric reinforced composites. Journal of Materials Processing Technology **55**(3), 171–177 (1995)

[9] Mouritz, A.P.: Tensile fatigue properties of 3d composites with through-thickness reinforcement. Composites Science and Technology **68**(12), 2503–2510 (2008)

[10] Tamuzs, V., Dzelzitis, K., Reifsnider, K.: Fatigue of woven composite laminates in off-axis loading i. the mastercurves. Applied Composite Materials **11**, 259–279 (2004)

[11] Tamuzs, V., Dzelzitis, K., Reifsnider, K.: Fatigue of woven composite laminates in off-axis loading ii. prediction of the cyclic durability. Applied Composite Materials **11**, 281–293 (2004)

[12] Stromeyer, C.E.: The determination of Fatigue Limits under Alternating Stress Conditions. Proceedings of the Royal Society of London. Series A **90**(620), 411–425 (1914)

[13] Moore, H.F., Kommers, J.B.: An Investigation of the Fatigue of Metals. New York **19**(8) (1921)

[14] Phong, L.: Fatigue limit evaluation of metals using an infrared thermographic technique. Mechanics of Materials **28**, 155–163 (1998)

[15] Doudard, C., Calloch, S., Hild, F., Cugy, P., Galtier, A.: Identification of the scatter in high cycle fatigue from temperature measurements. Comptes Rendus Mécanique **332**, 795–801 (2004)

[16] Le Saux, V., Marco, Y., Calloch, S., Doudard, C., Charrier, P.: Fast evaluation of the fatigue lifetime of rubber-like materials based on a heat build-up protocol and micro-tomography measurements. International Journal of Fatigue **32**, 1582–1590 (2010)

[17] Marco, Y., Masquelier, I., Le Saux, V., Charrier, P.: Fast prediction of the Wöhler curve from thermal measurements for a wide range of NR and SBR compounds. Rubber Chemistry and Technology **90**, 487–507 (2016)

[18] Serrano, L., Marco, Y., Le Saux, V., Robert, G., Charrier, P.: Fast prediction of the fatigue behavior of short-fiber- reinforced thermoplastics based on heat build-up measurements: application to heterogeneous cases. Continuum Mechanics and Thermodynamics **29**, 1113–1133 (2017)

[19] Meneghetti, G., Quaresimin, M.: Fatigue strength assessment of a short fiber composite based on the specific heat dissipation. Composites Part B: Engineering 42 **42**(2), 217–225 (2011)

[20] Munier, R., Doudard, C., Calloch, S., Weber, B.: Determination of high cycle fatigue properties of a wide range of steel sheet grades from self-heating measurements. International Journal of Fatigue **63**, 46–61 (2012)

[21] Sakagami, T., Kubo, S., Tamura, E., Nishimura, T.: Identification of Plastic-zone Based on Double Frequency Lock-in Thermographic Temperature Measurement. In: 11th International Conference on Fracture (ICF11), Turin, Italy (2005)

[22] Leveuf, L., Marco, Y., Le Saux, V., Navrátil, L.: Fast screening of the fatigue properties of thermoplastics reinforced with short carbon fibers based on thermal measurements fast screening of the fatigue properties of thermoplastics reinforced with short carbon fibers based on thermal measurements. Polymer Testing **68**, 19–26 (2018)

[23] Navrátil, L.: Apports de l'imagerie qualitative infrarouge pour la caractérisation thermomécanique et le dimensionnement en fatigue de composites tissés 3d. PhD thesis, ENSTA Bretagne (2021)

[24] InfraTec: ImageIR 10300 series. https://www.infratec.eu/thermography/infrared-camera/imageir-10300/ Accessed 2022-01-13

[25] Le Saux, V., Doudard, C.: Proposition of a compensated pixelwise calibration for photonic infrared cameras and comparison to classic calibration procedures: Case of thermoelastic stress analysis. Infrared Physics & Technology **80**, 83–92 (2017)

[26] Infrared, H.: Low temperature extended area blackbodies. https://hgh-infrared.com/dcn-1000-series/ Accessed 2022-01-13

[27] Poncelet, M.: Multiaxialité, hétérogénéités intrinsèques et structurales des essais d'auto-échauffement et de fatigue à grand nombre de cycles. PhD thesis (2007)

[28] Pitarresi, G., Found, M.S., Patterson, E.A.: An investigation of the influence of macroscopic heterogeneity on the thermoelastic response of fibre reinforced plastics. Composites Science and Technology **65**(2), 269–280 (2005)

[29] Dulieu-Smith, J.M., Quinn, S., Shenoi, R.A., Read, P.J.C.L., Moy, S.S.J.: Thermoelastic stress analysis of a grp tee joint. Applied Composite Materials **4**, 283–303 (1997)

[30] Pottier, T., Moutrille, M.P., Le Cam, J.B., Balandraud, X., Grédiac, M.: Study on the use of motion compensation techniques to determine heat sources. Application to large deformations on cracked rubber specimens. Experimental Mechanics **49**(4), 561–574 (2009)

[31] Chrysochoos, A., Huon, V., Jourdan, F., Muracciole, J.M., Peyroux, R., Wattrisse, B.: Use of full-field digital image correlation and infrared thermography measurements for the thermomechanical analysis of material behaviour. Strain **46**(1), 117–130 (2010)

[32] Chrysochoos, A., Berthel, B., Latourte, F., Galtier, A., Pagano, S., Wattrisse, B.: Local energy analysis of high-cycle fatigue using digital image correlation and infrared thermography. Journal of Strain Analysis for Engineering Design **43**(6), 411–421 (2008)

[33] Bodelot, L., Sabatier, L., Charkaluk, E., Dufrénoy, P.: Experimental setup for fully coupled kinematic and thermal measurements at the microstructure scale of an AISI 316L steel. Materials Science and Engineering A **501**(1-2), 52–60 (2009)

[34] Maynadier, A., Poncelet, M., Lavernhe-Taillard, K., Roux, S.: One-shot Measurement of Thermal and Kinematic Fields: InfraRed Image Correlation (IRIC). Experimental Mechanics **52**(3), 241–255 (2012)

[35] Sakagami, T., Yamaguchi, N., Kubo, S., Nishimura, T.: A new full-field motion compensation technique for infrared stress measurement using digital image correlation. The Journal of Strain Analysis for Engineering Design **43**(6), 539–549 (2008)

[36] Urbanek, R., Bär, J.: Influence of motion compensation on lock-in thermographic investigations of fatigue crack propagation. Engineering Fracture Mechanics **183**, 13–25 (2017)

[37] Padfield, D.: Masked object registration in the Fourier domain. IEEE

Transactions on Image Processing **21**(5), 2706–2718 (2012)

[38] van der Walt, S., Schönberger, J.L., Nunez-Iglesias, J., Boulogne, F., Joshua, W.D., Yager, N., Gouillart, E., Yu, T.: scikit-image: image processing in Python. PeerJ **2**, 453 (2014)

[39] Marco, Y., Le Saux, V., Jégou, L., Serrano, L., Launay, A., Raoult, I., Calloch, S.: Dissipation analysis in SFRP structural samples: Thermomechanical analysis and comparison to numerical simulations. International Journal of Fatigue **67**, 142–150 (2014)

[40] Doudard, C.: Détermination rapide des propriétés en fatigue à grand nombre de cycles à partir d'essais d'échauffement. PhD thesis (2004)

[41] Grady, L.: Random walks for image segmentation. IEEE Transactions on Pattern Analysis and Machine Intelligence **28**(11), 1768–1783 (2006)

[42] Chrysochoos, A.: Infrared thermography applied to the analysis of material behavior: a brief overview. Quantitative InfraRed Thermography Journal **9**, 193–208 (2012)